Minimizing molecular misidentification in imaging lowabundance protein interactions using spectroscopic singlemolecule localization microscopy

Yang Zhang,^{1,†} Gaoxiang Wang,^{1,2,†} Peizhou Huang,³ Edison Sun,¹ Junghun Kweon,¹ Qianru Li,^{1,4} Ji Zhe, ^{1,4} Leslie L. Ying,^{3,5}, and Hao F. Zhang^{1,*}

ABSTRACT: Super-resolution microscopy can capture spatiotemporal organizations of protein interactions with resolution down to 10 nm; however, the analyses of more than two proteins involving low-abundance protein are challenging because spectral crosstalk and heterogeneities of individual fluorescent labels result in molecular misidentification. Here we developed a deep learning-based imaging analysis method for spectroscopic single-molecule localization microscopy to minimize molecular misidentification in three-color super-resolution imaging. We characterized the 3-fold reduction of molecular misidentification in the new imaging method using pure samples of different photoswitchable fluorophores and visualized three distinct subcellular proteins in U2-OS cell lines. We further validated the protein counts and interactions of TOMM20, DRP1, and SUMO1 in a well-studied biological process - Staurosporine-induced apoptosis by comparing the imaging results with Western-blot analysis of different subcellular portions.

INTRODUCTION

Biological machinery often requires the interactions of more than two proteins at the nanoscale.1 In these multi-protein interactions (MPI), many proteins have an inherently low abundance. They are highly substoichiometric to their interaction counterparts either within the entire cell or in specific subcellular spaces with highly heterogeneous spatial distributions^{2, 3}. Traditional bioanalytical, biochemical, and biophysical approaches study these MPI at the ensemble level, mainly using preprocessed protein samples, while the spatial patterns are often overlooked.4 Imaging-based analyses offer an opportunity to investigate the spatiotemporal organization of proteins at the cellular and subcellular levels. Using fluorescence microscopy, researchers have shown the close relationship between the spatial distribution and the function of protein-protein interactions.⁵ However, the spatial resolution of conventional fluorescence imaging-based techniques is constrained by the optical diffraction limit to about 200 nm⁶. Although in situ proximity ligation assay (PLA)⁷ can capture the co-localizations of two proteins, imaging MPI at the nanoscale remains inaccessible.

Single-molecule localization microscopy (SMLM) overcomes the optical diffraction limit and offers a spatial resolution down to 10 nm.⁸⁻¹³ SMLM has been applied to study protein assemblies and interactions, including nuclear pore complexes¹⁴⁻¹⁶, centrioles¹⁷, and mitochondria-purinosomes interactions¹⁸. In addition, a few multiplexed SMLM experiments have been reported to study the distributions of multiple protein species using three photoswitchable fluorophores with minimal spectral overlaps. 19 Traditional SMLM uses selected optical filter sets to collect emission signals from distinctive spectral channels (Figure 1a). However, it is challenging to study MPI involving lowabundance proteins using traditional optical filter-based multiplexed SMLM. At the single-molecule level, spectral crosstalk between different fluorescent labels translates into a significant molecular misidentification rate (MMR) up to 8% between adjacent spectral channels. 19 Here, the MMR is defined as the number of single-molecule localizations misidentified in other channels divided by the total number of single-molecule localizations detected in all channels. A high MMR will cause incorrect visualization of subcellular structures (Figure S1 and Supplementary Note 1), inaccurate detection of low-abundance proteins, and misinterpretation of MPI (Figure S2).

¹ Department of Biomedical Engineering, Northwestern University, Evanston IL, 60208, USA

² Department of Hematology, Tongji Medical College, Huazhong University of Science and Technology, Wuhan Hubei, 430030, China

³ Department of Biomedical Engineering, The State University of New York at Buffalo, Buffalo, NY 14260, USA

⁴ Department of Pharmacology, Northwestern University, Chicago IL, 60611, USA

⁵ Department of Electrical Engineering, The State University of New York at Buffalo, Buffalo, NY 14260, USA

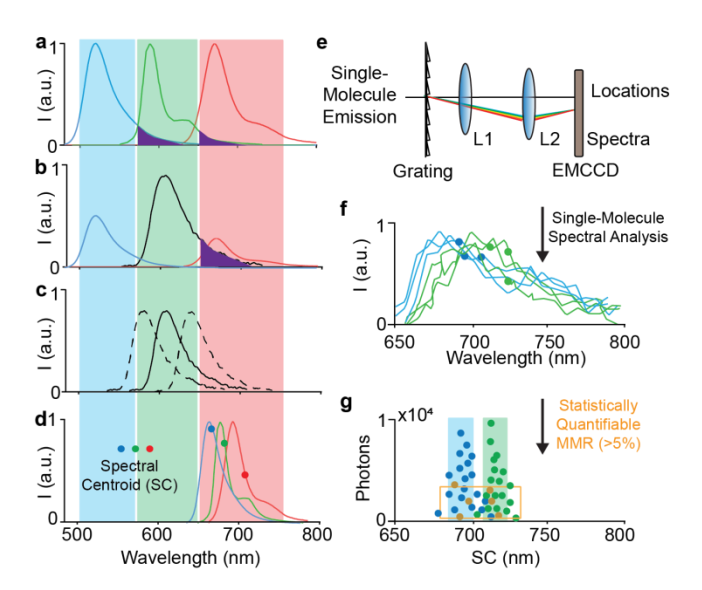


Figure 1. (a) An illustration of three-color SMLM based on multiple optical filter sets in the blue, green and red spectral channels; (b) the photon budget of the green dye is significantly higher than that of the red dye which further elevates MMR; (c) single-molecule fluorescence spectral heterogeneity causes spectral crosstalk; (d) concept of sSMLM to capture the full singlemolecule emission spectra, thus allowing the extraction of singlemolecule spectral centroid (SC); (e) a simplified schematic of the sSMLM optical setup: the collected single-molecule emission signals passes through an a transmission grating and a relay lens system (L1 and L2) to form the spatial and spectral images on an electron-multiplying charge-coupled device (EMCCD); (f) representative single-molecule emission spectra and SC of two molecular species (green and blue); (g) An illustrative scatterplot of photon vs. SC of single-molecules from two fluorophore species with the misidentified single-molecules shown in the yellow-boxed region.

Furthermore, despite sequential labeling strategies that can image different molecular targets, ^{20,21} the complicated imaging procedures and unwashed labels leftover from the previous labeling cycles could also lead to elevated MMR. Therefore, it is crucial to minimize MMR in multiplexed SMLM for studying MPI involving low-abundance proteins.

Two main sources can elevate MMR in multiplexed SMLM. First, different fluorophore species have varied photon budgets. ¹⁹ The high-photon-budget fluorophores can cause increased single-molecule signal bleed-through to the adjacent channels that are used for detecting a relatively low-photon budget fluorophore (Figure 1b). Second, single-molecule fluorescence spectral heterogeneity from the same type of fluorophores causes spectral variations up to ~50 nm.²² This intrinsic property can also result in higher spectral crosstalk in SMLM (Figure 1c) and also conventional multi-color fluorescence microscopy by broadening the ensemble-averaged emission spectra.⁶ These two types of crossed-channel single-molecule signals will be treated as single-molecule emission events in the adjacent channels in SMLM, leading to false single-molecule localization and elevated MMR.

Recently, we and other groups developed spectroscopic SMLM or sSMLM, which concurrently captures the emission spectra and spatial locations of individual fluorescent molecules²³⁻²⁶ (Figures **1d-e** and **S3**). By discriminating single-molecule spectral features (*e.g.*, spectral centroids³⁷, Figure **1d**), sSMLM

permits simultaneous multiplexed SMLM regardless of spectral overlap.³¹ In addition, sSMLM allows measuring single-molecule fluorescence spectral heterogeneity in a high-throughput manner and guides the selection of photoswitchable fluorophores.²² Nevertheless, existing molecular classification methods in sSMLM analyze a few discrete spectral signatures (e.g., spectral peaks or centroids) from one-dimensional (1D) single-molecule spectra. These processed 1D spectral signals are noisy because of the elevated imaging background and limited single-molecule photon budget (Figure 1f).²⁷ As a result, current sSMLM exhibits an MMR of ~5% between adjacent spectral centroid bands (Figure 1g) ^{23,24,28}.

We illustrate the impact of MMR on imaging the MPI (Figure 2) using the MPI involving small ubiquitin-like modifier 1 (SUMO1), dynamin-related protein 1 (DRP1), and TOMM20 (mitochondria outer membrane marker) as a biologically significant example. SUMO1 is a classical post-translational modifier that can attach to and modify the functions of their interacting counterparts during transcriptional regulation, nucleoplasmic transport, and apoptosis. 4,29,30 Increasing evidence has shown their essential roles in the cytoplasmic region where SUMO1 has relatively low expression levels^{31,32} and is highly substoichiometric to the interacting counterparts.³³ Specifically, SUMO1 has been well-established for its role in apoptosis while interacting with mitochondria and DRP1, a protein essential for controlling mitochondria fission.¹⁰ During apoptosis, the DRP1-mitochondria interaction pattern shifted from rapid cycling to enhanced interaction and even permanent contact before losing mitochondrial membrane potential (Figures 2a-b). The stabilization of DRP1 to mitochondrial membrane is stimulated by post-translational modification of SUMO1 to DRP1 (illustrated as more colocalization between SUMO and DRP1 on mitochondria Figure 2b).

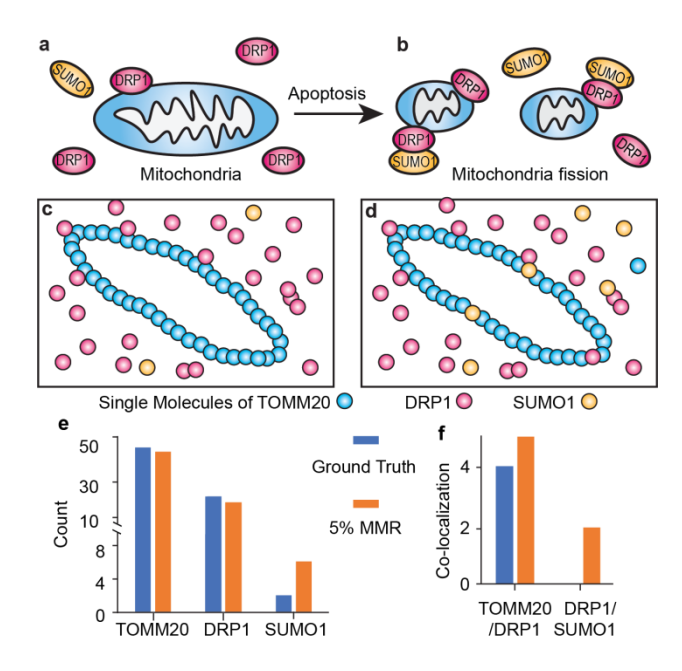


Figure 2. (**a-b**) A schematic illustration of MPI among TOMM20, DRP1, and SUMO1 (**a**) before and (**b**) after programmed apoptosis. (**c**) An illustrative three-color SMLM image of TOMM20, DRP1, and SUMO1 with 0% MMR (or ground truth), and (**d**) with 5% MMR; (**e-f**) the number of detected TOMM20, DRP1, and SUMO1 molecules (**e**) and the number of co-localization (**f**) between DRP1 and SUMO1 and between DRP1 and TOMM20, in **c** and **d**, respectively

We illustrate the influence of elevated MMR on mispresenting MPI among SUMO1, DRP1, and the mitochondria membrane marker TOMM20. In the ground-truth SMLM image with 0% MMR, only 2 low-abundance SUMO1 proteins are present and randomly distributed in the imaging field-of-view (FOV) (Figure 2c). Suppose the SMLM system has a 5% MMR; in that case, the detected number of SUMO1 proteins and the colocalization patterns among the three proteins can vary drastically (Figure 2d). For instance, the number of SUMO1 is overestimated by 3 times (Figure 2e). Two co-localization between DRP1 and SUMO1 could be falsely detected (Figure 2f). Using numerical simulations, we further investigated that MMR can significantly affect the accuracy of detecting single molecules and visualizing MPI (Figure S4 and Supplementary Note 2).

To minimize MMR, we rationalize that the raw twodimensional (2D) single-molecule spectral images captured in sSMLM contain rich, high-dimensional information³⁴ of molecular signatures that are overlooked by the existing classification algorithm in sSMLM. Particularly, preprocessed 1D spectral data only represent the correlation between the adjacent wavelengths. In contrast, raw 2D spectral images might contain fluorophore-dependent spectral and spatial point spread functions as well as signal-to-noise ratios. The implementations of deep learning convolutional neural networks have demonstrated outstanding performance in general imaging classification tasks³⁵ and reported to extract invaluable information from individual raw frames and reconstructed images in SMLM for molecular classification^{34,36}, background estimation³⁷, and imaging speed acceleration³⁸. We previously developed an artificial neural network-based spectral classification method to classify two-color sSMLM images.³⁶ However, our attempts using this simple network to classify three fluorescent labels failed with <85% accuracy. In this work, we report an imaging workflow involving a deep learning neural network to classify full single-molecule spectral images of fluorescent labels obtained from sSMLM, referred to as SpeNet. We demonstrated MMR reduction in three-color sSMLM imaging of fixed cells. We further benchmarked SpeNet's performance in sSMLM imaging of complex MPIs among TOMM20, DRP1, and SUMO1 in apoptosis at the single-cell level for the first time.

MATERIALS AND METHODS

Cell Preparation. HeLa and U2-OS cells (ATCC) were grown in Dulbecco's Modified Eagle Media (DMEM, ThermoFisher) and McCoy's 5A Medium (ATCC@-30-2007TM), respectively supplemented with 2 mM L-glutamine (ThermoFisher), 10% fetal bovine serum (FBS, ThermoFisher), and 1% penicillin/streptomycin (100 U mL⁻¹, ThermoFisher) at 37°C with 5% CO₂. The cells were seeded 8-well Chambered Coverglass (NuncTM Lab-TekTM) with 50-70% confluency. 24-48 hours after plating, the cells were fixed in pre-warmed 3% Paraformaldehyde and 0.1 % Glutaraldehyde in Phosphate Buffer Saline (PBS,) for 10 min. The cells were washed with PBS, quenched with freshly prepared 0.1 % NaBH₄ in PBS for 7 min, rinsed with PBS three times at 25 °C, and stored at 4°C for imaging within a week.

To induce cell apoptosis in HeLa cells, we seeded HeLa cells on 8-Well Chambered cover glass for 48 h and incubated them with 10 μ M Staurosporine (STS) (Abcam #120056) in DMSO for 2 h at 37 °C. The volume of DMSO added to each well was

5 μ L. For the control group, the equivalent amount of DMSO was added to the cells without STS.

U2-OS or HeLa cells were then labeled using immunofluorescence staining before sSMLM imaging. Generally, the fixed cells were permeabilized with a blocking buffer (3% Bovine Serum Albumin (BSA), 0.5% Triton X-100 in PBS) for 20 min at 25 °C and then incubated with the primary antibodies at optimal dilutions overnight in blocking buffer overnight at 4°C and rinsed with a washing buffer (0.2% BSA, 0.1% Triton X-100 in PBS) for three times. The cells were further incubated with corresponding secondary antibody-dye conjugates for 40 min, washed thoroughly with PBS three times at 25 °C, and stored at 4 °C. Antibody concentrations and sources are listed in Table S1.

Imaging acquisition and processing. The schematic of our sSMLM optical system was described previously 27 and shown in Figure S3. Prior to imaging, an imaging buffer (400 μL) containing 50 mM Tris (pH = 8.0), 10 mM NaCl, 0.5 mg/mL Glucose Oxidase (Sigma, G2133), 2000 U/mL Catalase (Sigma, C30), 10% (w/v) D-Glucose, and 100 mM Cysteamine was added to the cell sample. We respectively recorded 5,000, 10,000, and 30,000 frames for imaging IgG-dye conjugates adsorbed on glass, the three-color imaging of HeLa cells, and three-color imaging of U2-OS cells with a frame exposure time of 20 ms.

The spatial localization of each single-molecule blinking event was calculated using ThunderSTORM⁵¹. To obtain the full emission spectral images of single molecules, a spectral collection range of 600 – 800 nm was selected, and a (16-19) ×7 pixel area on an imaging frame that corresponds to the spectral image region was cropped with the spatial information of the single-molecules as the reference using a pre-measured calibration process.²². The variation of the pixel area is caused by slightly different spectral dispersion values (5-7 nm) in spectrometer alignment processes.²⁷ The 2D spectral images were then interpolated to 201 ×7 pixels and normalized to [0-1] values for training and testing SpeNet.

Sample preparation for training and independent validation datasets for SpeNet. The experimental training dataset was collected by imaging three different samples, each containing dye-IgG proteins of Alexa Fluor 647 (647), Biotium CF660C (660), or Biotium 680 (680) adsorbed on glass substrates. Briefly, 2 μg mL $^{-1}$ of 647, 660, or 680 IgG conjugates in PBS (200 μL) were added to Poly-L-Lysine (PLL)-coated 8-well chambered cover glass for 5 min. The glass was then rinsed thoroughly with PBS, and 200 μL of fresh-prepared imaging buffer was used to replace PBS before imaging acquisition. For each sample, we acquired 5-7 different FOV at different regions of the glass substrate, which provided $\sim 10^6$ single-molecule blinking events as the ground truth for each dye species.

SpeNet training, independent validation, and post-classification processing. The SpeNet architecture consists of 13 layers described and is implemented using Matlab with a graphic card (Nvidia GeForceGTX1070) and CUDA9.0. To clean up the data, we rejected the molecules with the Pearson correlation coefficient (C) < 0 between each single-molecule spectrum and each of the three averaged emission spectra. We randomly allocated 80% ($\sim 1.2 \times 10^5$ single-molecule spectral images) of the clean data as a training dataset and kept the rest 20% as an initial testing dataset. The spectral images acquired from pure dye samples prepared provided the ground truth for

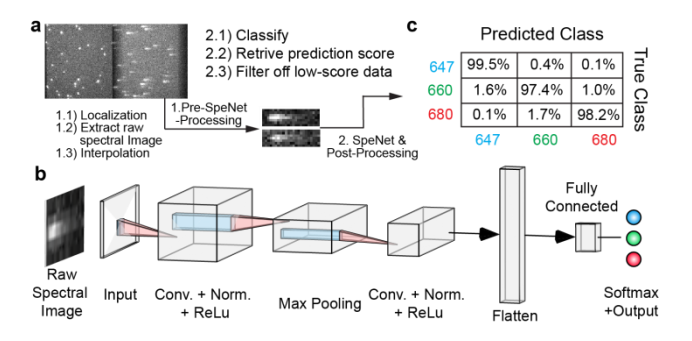


Figure 3. (a) Post-sSMLM-imaging for sSMLM before and after SpeNet processing; **(b)** The architecture of SpeNet; **(c)** Confusion matrix of SpeNet using independently acquired data.

single-molecule spectral images as we know the prerequisite information of the origin of each spectral image.

For network training, 25 Epochs were tested for network convergence. The neural network converged at 87% accuracy on the initial testing data. After the neural network was trained, we performed an independent validation using separately acquired data. We further filtered out low-quality spectral images after SpeNet analyzed the spectral images using the prediction score parameter (<0.8) in the output. By applying a different prediction score filter, the MMR can be reduced to 0.5% at the expense of rejecting more localization events.

RESULTS AND DISCUSSION

SpeNet for high-accuracy single-molecule spectral classification. In our previous studies, we showed that our grating-based sSMLM could achieve simultaneous three-color super-resolution imaging using 647, 660, and 680 dyes with 5% MMR. ³⁶ Such MMR is sufficient to distinguish different protein markers of subcellular organelles highly abundant in cells but can be challenging to distinguish any low-abundance proteins (Figures S1-S2). Using numerical simulation, we simulate two randomly distributed proteins with varying expression levels (Supplementary Note 2 and Figure S4). We found that a 5% MMR resulted in a 2-fold reduction of the degree of colocalization (DoC) in coordinate-based co-localization analysis³⁹ when one protein expression level is 10-fold lower than the interacting counterpart. To measure the DoC of substoichiometric interacting protein pairs accuracy >90% in such conditions, the MMR needs to be less than 2% (Figure S4).

To minimize MMR, we develop a post-imaging workflow (Figure 3a) by creating a SpeNet deep neural network to classify the full single-molecule fluorescence spectral images of 647, 660, and 680, which are routinely used for three-color sSMLM. We did not use photoswitchable fluorescent proteins because of their relatively large single-molecule spectral diffusion over time and single-molecule spectral heterogeneity, and relatively lower photon budget.²⁶ The workflow has two main steps: (1) data preprocessing as inputs for SpeNet, including single-molecule localization as previously described²⁷, extracting raw spectral images and imaging interpolation, and (2) SpeNet classification and post-SpeNet processing to filter out data with low prediction scores. The architecture of SpeNet consists of 13 layers, including a convolutional layer with a filter size of 5×5 and 8 features (8, 5×5), a normalization layer, a Rectified Linear Unit (ReLu) layer to solve the vanishing gradient problem⁴⁰, a max-pooling layer (3×3) to enhance the features, a convolutional layer (8,

3×3), a normalization layer, a ReLu layer, a flattening layer, a sequential fully connected layer, a softmax layer, and an output layer (Figure 3b).

We first trained the SpeNet using experimentally acquired data by imaging pure 647, 660, and 680 dye-IgG conjugates adsorbed on PLL-coated glass substrates. We used PLL-coated substrates other than single-color labeled cells because of their lower background autofluorescence signals than cell samples, where the background autofluorescence might contaminate the training dataset. Moreover, using PLL-coated substrates lead to relatively easy sample preparation to provide controllable, sparse, and non-overlapping single-molecule spectral image density to ensure the quality of the training data. We also compared the statistical distribution of spectral centroids of the three dyes on the PLL-coated substrates with those labeled directly in cells (Figure S5), and we found that the histograms closely resemble each other. Using separately prepared samples, we characterized the classification performance of SpeNet using a confusion matrix (Figure 3c). As the spectral overlaps between 660 and 647 and between 660 and 680 were relatively high (Figure S6A), SpeNet gave relatively high MMRs of 1.6% and 1.7%, while the MMR between 647 and 680 was <0.1%. Compared with the original SC method, SpeNet reduced the MMR by 3-11 times among adjacent channels.

Validating SpeNet in three-color sSMLM imaging of U2-OS cell. We tested SpeNet's performance in classifying three-color sSMLM data of immunofluorescence-labeled U2-OS cells. We respectively stained three intracellular proteins, including TOM20, Tubulin, and Peroxisome membrane marker PMP70, with 647, 660, and 680. As shown in Figures 4a-4d, the sSMLM images classified by SpeNet showed exclusive morphologies of tubulovesicular structures (Figure 4b), linear filaments (Figure 4c), and worm-like cluster patterns (Figure 4d) in the separately displayed sSMLM images that show exclusively identified the molecules belonging to 647, 660, and 680 classes. These visualized distinct morphologies agree with the typical morphologies of mitochondria, tubulin, and peroxisomes. The average localization precision and Fourier ring correlation

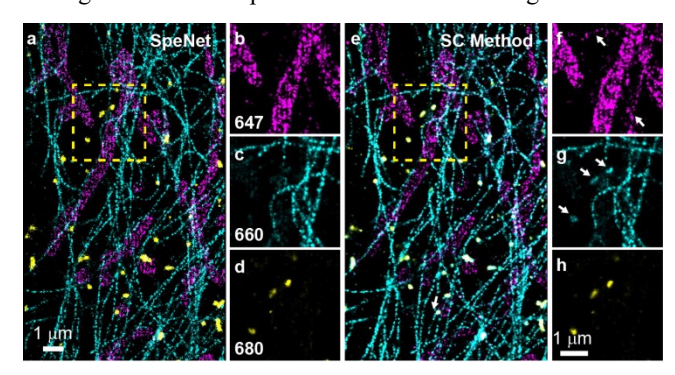


Figure 4. (a) sSMLM images of a fixed U2-OS cell processed using SpeNet (a-d) and SC Method (e-h). The mitochondria (magenta), tubulin (cyan), and peroxisome (yellow) of the cell are immunofluorescence-labeled with 647, 660, and 680, respectively. The overlaid three-color sSMLM images show significantly reduced misidentifications in the SpeNet (a) compared to the SC Method (e). The separately displayed three-color images (b-d and f-h) are magnified views of the dashed rectangular region in panels a and e, respectively. Panels b-d show distinct tubulovesicular, linear and worm-like morphologies of mitochondria, tubulin, and peroxisomes, respectively, with SpeNet classification. The arrow-pointed linear features in mitochondria (f) and worm-like features in tubulin (g) indicated the misidentified molecules using SC Method.

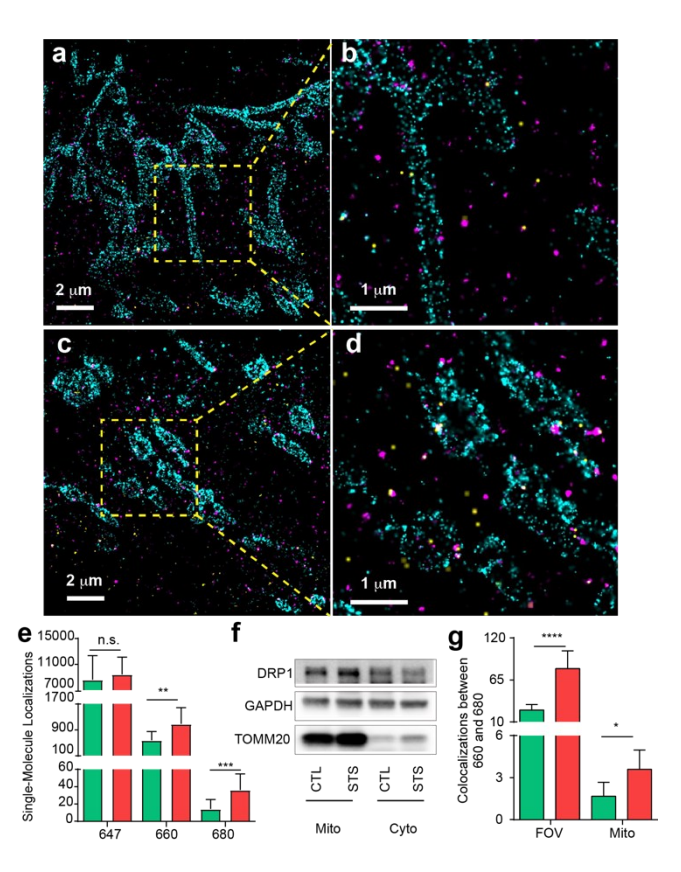


Figure 5. Representative overlaid three-color sSMLM images (**a-d**) and single-cell analyses (**e-g**) of HeLa cells before (**a-b**) and after (**c-d**) STS treatment for 2 hours; TOM20 (cyan), DRP1 (magenta), and SUMO1 (yellow) were respectively labeled with 647, 660, and 680; (**b** and **d**) are the magnified view of the square box in **a** and **c** respectively. (**e**) The comparisons of total counts of 647, 660, and 680 single-molecule localizations between CTL and STS groups in mitochondrial fractions. (**f**) Western blots result from HeLa cells treated with DMSO or STS; (**g**) The number of colocalization between DRP1 and SUMO1 from sSMLM data in the entire imaging field of view and associated with mitochondria. (N = 15 for each group)

(FRC) resolution are \sim 25 nm and \sim 75 nm, respectively (Figure S7).

We also processed the same sSMLM image using the SC method (Figures 4e-4h). The overlaid three-color sSMLM image (Figure 4e) showed significant color overlapping in the highlighted region. In addition, the separately displayed sSMLM images revealed unexpected linear (Figure 4f) and worm-like patterns (Figure 4g) in the arrow-pointed regions in 647 and 660 windows, respectively. Similarly, we also observed more molecular misidentifications in the CF680 channel but different contrast visualization (Figures S6C, D). Based on the reported biological characteristics of TOMM20 and Tubulin proteins, the assemblies of TOMM20 and tubulin should not form linear and worm-like patterns. Instead, these unexpected patterns were falsely created due to a higher MMR in the SC method. In short, these imaging results of cell samples validated that SpeNet can reduce MMR in sSMLM images.

Three-color sSMLM imaging of MPI among SUMO1, DRP1, and TOMM20 in healthy and early apoptotic HeLa cells. We further tested SpeNet in classifying sSMLM images of MPI among SUMO1, DRP1, and TOMM20 during apoptosis by treating HeLa cells with 10- μ M STS for 2 hours. 31 We

respectively immunolabeled the TOMM20, DRP1, and SUMO1 proteins with 647, 660, and 680 dyes. We also prepared a control group (CTL) without STS treatment under identical conditions. In CTL, the sSMLM image of TOM20 (pseudo-colored in cyan in Figures 5a-5b) revealed consistent tubulovesicular structures compared with the ones shown in Figure 4 as well as other reported mitochondria SMLM images. DRP1 and SUMO1 (respectively pseudocolored as magenta and yellow in Figure 5b) are distributed throughout the FOV, while the number of cytosolic SUMO1 localizations is significantly lower than the number of DRP1 localizations. In STS, we observed mitochondria fission to more discontinued and circular patterns (Figures 5c-5d), consistent with the literature report.

We quantified the total number of detected fluorescent localizations as a measure of the number of targeted proteins in CTL and STS. It has been well-known that the number of detected localizations from the fluorescent label is proportional to the expression level of the target protein. 42,43 We assumed that the primary and secondary antibody labeling efficiency did not change in CTL and STS groups and further examined the spatial interactions among DRP1, SUMO1, and TOM20 at different subcellular locations. Specifically, the average total numbers of detected localizations per cell associated with the mitochondria for TOMM20, DRP1, and SUMO1 were 8603, 577, and 14 in the CTL group and 9445, 1083, and 36 in the STS group, respectively (Figures 5e). Applying the student's t-test, we found that the TOMM20 expressions had no statistical difference between the STS and CTL groups. The DRP1 and SUMO1 expressions respectively increased by 1.9-fold and 2.5fold in the STS group compared with the CTL group with the statistical powers greater than 0.95 using the G*Power software.44 These values agree well with reported biochemical studies.31 For independent validation using Western blot, the count of TOMM20 did not alter in the CTL and STS groups, but DRP1 showed higher expression levels in the mitochondrial fraction (Figure 5f). Meanwhile, the cytosol showed a minimal amount of TOMM20 signal in the Western blot assay, suggesting the successful separation of mitochondrial fraction from the cytosol.

Lastly, we quantified the co-localization between DRP1 and SUMO1 associated with mitochondria and in the entire FOV. The numbers of co-localization between DRP1 and SUMO1 in the FOV increased by 2.1-fold in the STS group than in the CTL group (Figure 5g). The numbers of DRP1-SUMO1 colocalization associated with mitochondria also increased by 2.3fold in the STS group than in the CTL group. In addition, since DRP1 is reported to form aggregates, we performed a densitybased spatial clustering analysis of applications with noise (DBSCAN⁴⁵) on the 660 channel to investigate DRP1's oligomerization statuses in CTL and STS (Figure S8). A representative two-color sSMLM image (Figure S8B) of mitochondria and DRP1-Oligomers indicated that the majority of DRP1-Oligomers (18 out of 22 detected oligomers) were associated with mitochondria. Furthermore, some of the DRP1-Oligomers are located at the constriction sites of mitochondria, which implicates a unique function of DRP1-Oligomers in mitochondria fission (Arrow-pointed regions in Figure S8B).⁴⁶ These results indicate the capability of sSMLM and SpeNet in analyzing spatially-resolved MPI involving low-abundance proteins at the single-molecule level.

The above results showed that SpeNet could classify 647, 660, and 680 labels with an MMR of <= 1.7%. To achieve this, SpeNet rejected a large portion of the detected localizations, which might affect the reconstructed image quality associated with the Nyquist sampling theorem. 47 To assess this effect, we first calculated the localization utilization ratio (LUR) 48, which is defined as the total number of remaining localizations after classification divided by the total number of identified spatial localizations from the spatial images. For all the processed sSMLM cell imaging datasets, the LURs are ~15-25%, which is reduced from ~40-60% in sSMLM classification based on the SC method. ²⁷ We also compared the classification accuracies of SpeNet at various photon count levels and found that photon count thresholds of > 2000 and of <1000 provide 98.5% and 84% accuracies, respectively (Figure S9). The dimmer localizations are mostly filtered out in SpeNet to reach the >98.3% classification accuracy. However, as we mentioned previously. simple photon thresholding in the SC method does not yield similar classification accuracies. 24,27 Presumably, the photon count is a highly weighted parameter in SpeNet, while additional high-dimensional features also contribute to the improved classification performance.^{37,40} We further measured the Fourier ring correlation (FRC) resolution of the reconstructed sSMLM images using the SpeNet. It shows a similar FRC resolution of ~80 nm compared to the original image (Figure S6B). Presumably, more than 2 million detected single-molecules in the original image sequence provide a large pool of redundant single-molecule localizations to reconstruct the final image. It also implies that the sSMLM imaging acquisition speed could potentially be increased by acquiring a smaller number of frames with a sufficient but non-redundant number of single-molecule localization.

Second, the statistical analyses suggest the expression level of TOMM20 remains unchanged after the treatment with STS while DRP1 and SUMO were respectively upregulated by 1.5fold and 2.5-fold during the STS-induced apoptosis process in mitochondrial fractions. We note that each fluorescent label has distinct blinking photophysics, which could cause variations when converting the localization counts to protein counts. 49 However, for the same fluorescent labels illuminated under identical imaging conditions, each fluorescent label's blinking dynamics remain unchanged.¹⁹ We also assumed that the antibody labeling efficiency remained unchanged in the CTL and the STS groups under identical conditions. With these considerations, we believe that the ratio of the blinking counts can indicate the relative changes in protein counts. Indeed, from our single-cell imaging analysis, both DRP1 and SUMO1 were upregulated during apoptosis, consistent with literature precedents using western blots and confocal microscopy. 31,50 In short, sSMLM allows the relative quantification of TOM20, DRP1, and SUMO1 expression levels during the apoptosis process at the single-cell level.

Third, when studying spatial interactions among the three proteins, the 3D coordinate of every single molecule should be ideally captured to unambiguously reveal the spatial colocalizations. However, it is practically challenging to implement 3D, three-color sSMLM for present studies because of relatively low throughput, degraded lateral resolution, potential inaccurate spatial localization, spectral calibration errors, and elevated MMR in current 3D sSMLM modalities. ^{24,48} To circumvent these issues, we performed a 2D three-color sSMLM imaging, which provides a projection of a 3D object to capture a slice of ~300 nm by rejecting defocused PSF to

capture the co-localizations. We used a control sample made from fluorescent nanospheres to determine the relationship between the standard deviation (σ) of single-molecule point-spread function and relative z-position to the sample focal plane (Figure S10). By rejecting localizations whose σ is larger than 150 nm, we confined the axial range of the 2D sSMLM image to a 300-nm slice. We also performed numerical simulations to assess the influence of the 2D projection of a 3D slice in realistic localization densities detected in the experiment (Figures S11-S12 and Supplementary Note 3). These simulation results validated that the 2D-sSMLM projection of a 300-nm slice can be sufficient to analyze protein interactions of DRP1, SUMO1, and TOM20 under our experimental condition.

CONCLUSION

We developed a deep-learning neural network-based singlemolecule spectral classification method (SpeNet) for identifying three fluorescent labels (647, 660, and 680) used in sSMLM with an MMR <=1.7%. We demonstrated the classification performance by sSMLM imaging of three subcellular structures (mitochondria, tubulin, and peroxisomes) of immunofluorescence-labeled U2-OS cells. Furthermore, we used SpeNet to classify sSMLM data of three-protein colocalization among DRP1, SUMO1, and TOMM20 under healthy and STS-induced apoptotic conditions. SpeNet allowed the identification of low-abundance SUMO1 and the analyses of coordinate-based co-localization. The changes in protein expression and co-localization levels agreed well with the reported biochemical results. Using sSMLM and SpeNet, we revealed ~1.5-fold increases in mitochondria-associated DRP1 and 2.5-fold SUMO1 signals.

Developing deep-learning neural networks in sSMLM correlating the spatial and spectral images at pre-and postimaging-reconstruction levels may provide invaluable information for high-fidelity molecular discrimination beyond existing capabilities. In fact, we anticipate that SpeNet should, in principle, perform better for classifying more dye molecules (or more than 3 color channels) because of its ability to discriminate the high-dimension features of dye molecules. The existing challenge is the identification of more dyes that can work simultaneously under identical sSMLM imaging conditions and have low single-molecule fluorescence spectral heterogeneity. Furthermore, the synergistic interplay of brighter and multiplexed fluorescent labels, efficient optical systems to utilize the precious photon budget, and sophisticated postimaging-processing method would fully unleash the power of sSMLM for high-throughput, 3D, highly multiplexed superresolution mapping of complex protein interactions.

ASSOCIATED CONTENT

Supporting Information

The Supporting Information is available free of charge on the ACS Publications website.

Additional experimental and simulated SMLM images; antibody information; simulation for MMR effects, 3D calibration experimental and simulated data, optical setup, and FRC resolution and localization precision (PDF).

The source code for implementing SpeNet is available on Github (https://github.com/FOIL-NU/SpeNet) and the original imaging datasets are available upon request to the corresponding author.

AUTHOR INFORMATION

Corresponding Author

*hfzhang@northwestern.edu

Author Contributions

† Y. Z. and G. W. contributed equally to this work.

Y. Z., G. W, and H. F. Z. conceived the project, Y. Z. and P. H. developed the classification network, Y. Z. and J. K. performed U2-OS cell imaging experiments. Y. Z. and G. W. designed protein interaction studies during apoptosis and performed HeLa cell imaging experiment, Q. L., J. K., and J. Z. performed Western blot assay, Y. Z., E. S., G. W., and H. F. Z. analyzed the data, Y. Z., G. W., L. Y., and H. F. Z wrote the manuscript.

Notes

The authors declare no competing financial interest.

ACKNOWLEDGMENT

We acknowledge the generous support from the National Science Foundation grants CHE-1954430 and EFRI-1830969, and the National Institutes of Health grants R21GM141675, R01EY026078, R01EY019949, R01GM140478, R01GM139151, R01GM143397, and U54CA268084.

REFERENCES

- Wilson, W. D. Analyzing Biomolecular Interactions. Science 2002, 295, 2103.
- (2) da Costa, J. P., Santos, P. S. M., Vitorino, R., Rocha-Santos, T. & Duarte, A. C. How low can you go? A current perspective on lowabundance proteomics. *Trends Anal. Chem.* 2017, 93, 171-182.
- (3) Fleissner, F., Bonn, M. & Parekh, S. H. Microscale spatial heterogeneity of protein structural transitions in fibrin matrices. Sci. Adv. 2016, 2, e1501778.
- (4) Song, J., Durrin, L. K., Wilkinson, T. A., Krontiris, T. G. & Chen, Y. Identification of a SUMO-binding motif that recognizes SUMO-modified proteins. *Proc. Natl. Acad. Sci. U. S. A.* 2004, 101, 14373-14378.
- (5) Nevo-Dinur, K., Govindarajan, S. & Amster-Choder, O. Subcellular localization of RNA and proteins in prokaryotes. Trends Genet. 2012, 28, 314-322.
- (6) Moerner, W. E. Single-Molecule Spectroscopy, Imaging, and Photocontrol: Foundations for Super-Resolution Microscopy (Nobel Lecture). Angew. Chem. Int. Ed. Engl. 2015, 54, 8067-8093
- (7) Ristic, M., Brockly, F., Piechaczyk, M. & Bossis, G. Detection of Protein-Protein Interactions and Post-translational Modifications Using the Proximity Ligation Assay: Application to the Study of the SUMO Pathway. *Methods Mol. Biol.* 2016 1449, 279-290.
- (8) Rust, M. J., Bates, M. & Zhuang, X. Sub-diffraction-limit imaging by stochastic optical reconstruction microscopy (STORM). *Nat. Meth.* 2006, 3, 793-796.
- (9) Betzig, E. *et al.* Imaging Intracellular Fluorescent Proteins at Nanometer Resolution. *Science* **2006**, 313, 1642.
- (10) Hell, S. W. Nanoscopy with Focused Light (Nobel Lecture). Angew. Chem. Int. Ed. Engl. 2015, 54, 8054-8066,
- (11) Gustafsson, M. G. L. Nonlinear structured-illumination microscopy: Wide-field fluorescence imaging with theoretically unlimited resolution. *Proc. Natl. Acad. Sci. U. S. A.* 2005, 102, 13081-13086.
- (12) Sharonov, A. & Hochstrasser, R. M. Wide-field subdiffraction imaging by accumulated binding of diffusing probes. *Proc. Natl. Acad. Sci. U. S. A.* 2006, 103, 18911-18916.
- (13) Sigal, Y. M., Zhou, R. & Zhuang, X. Visualizing and discovering cellular structures with super-resolution microscopy. *Science* 2018, 361, 880.
- (14) Szymborska, A. et al. Nuclear Pore Scaffold Structure Analyzed by Super-Resolution Microscopy and Particle Averaging. Science 2013, 341, 655.

- (15) Meijering, E., Carpenter, A. E., Peng, H., Hamprecht, F. A. & Olivo-Marin, J. C. Imagining the future of bioimage analysis. *Nat. Biotechnol.* 2016, 34, 1250-1255.
- (16) Loschberger, A. *et al.* Super-resolution imaging visualizes the eightfold symmetry of gp210 proteins around the nuclear pore complex and resolves the central channel with nanometer resolution. *J. Cell Sci.* **2012**, 125, 570-575.
- (17) Fu, J. & Zhang, C. Super-resolution microscopy: successful applications in centrosome study and beyond. *Biophysics Reports* 2019, 5, 235-243.
- (18) French, J. B. *et al.* Spatial co-localization and functional link of purinosomes with mitochondria. *Science* **2016**, 351, 733-737.
- (19) Dempsey, G. T., Vaughan, J. C., Chen, K. H., Bates, M. & Zhuang, X. Evaluation of fluorophores for optimal performance in localization-based super-resolution imaging. *Nat. Meth.* 2011, 8, 1027-1036.
- (20) Agasti, S. S. et al. DNA-barcoded labeling probes for highly multiplexed Exchange-PAINT imaging. Chem. Sci 2017, 8, 3080-3091
- (21) Jungmann, R. *et al.* Multiplexed 3D Cellular Super-Resolution Imaging with DNA-PAINT and Exchange-PAINT. *Nat. Meth.* **2014**, 11, 313-318.
- (22) Zhang, Y. et al. Investigating Single-Molecule Fluorescence Spectral Heterogeneity of Rhodamines Using High-Throughput Single-Molecule Spectroscopy. J. Phys. Chem. Lett., 2021, 3914-3921.
- (23) Dong, B. et al. Super-resolution spectroscopic microscopy via photon localization. Nat. Commun. 2016, 7, 12290.
- (24) Zhang, Z., Kenny, S. J., Hauser, M., Li, W. & Xu, K. Ultrahighthroughput single-molecule spectroscopy and spectrally resolved super-resolution microscopy. *Nat. Methods* 2015, 12, 935-938.
- (25) Bongiovanni, M. N. et al. Multi-dimensional super-resolution imaging enables surface hydrophobicity mapping. Nat. Commun., 2016, 7, 13544.
- (26) Mlodzianoski, M. J., Curthoys, N. M., Gunewardene, M. S., Carter, S. & Hess, S. T. Super-Resolution Imaging of Molecular Emission Spectra and Single Molecule Spectral Fluctuations. *PLoS ONE* 2016, 11, e0147506.
- (27) Zhang, Y. et al. Multicolor super-resolution imaging using spectroscopic single-molecule localization microscopy with optimal spectral dispersion. Appl. Opt. 2019, 58, 2248-2255.
- (28) Kim, D., Zhang, Z. & Xu, K. Spectrally Resolved Super-Resolution Microscopy Unveils Multipath Reaction Pathways of Single Spiropyran Molecules. J. Am. Chem. Soc., 2017, 139, 9447-9450.
- (29) Gareau, J. R. & Lima, C. D. The SUMO pathway: emerging mechanisms that shape specificity, conjugation and recognition. *Nat. Rev. Mol. Cell Biol.*, 2010, 11, 861-871.
- (30) Geiss-Friedlander, R. & Melchior, F. oncepts in sumoylation: a decade on. *Nat. Rev. Mol. Cell Biol.*, **2007**, 8, 947-956.
- (31) Wasiak, S., Zunino, R. & McBride, H. M. Bax/Bak promote sumoylation of DRP1 and its stable association with mitochondria during apoptotic cell death. *J. Cell Biol.*, 2007, 177, 439-450.
- (32) Choi, S. G. et al. SUMO-Modified FADD Recruits Cytosolic Drp1 and Caspase-10 to Mitochondria for Regulated Necrosis. Mol. Cell Biol., 2017, 37, e00254-16.
- (33) Prudent, J. et al. MAPL SUMOylation of Drp1 Stabilizes an ER/Mitochondrial Platform Required for Cell Death. Mol. Cell 2015, 59, 941-955.
- (34) Kim, T., Moon, S. & Xu, K. Information-rich localization microscopy through machine learning. *Nat. Commun.*, 2019, 10, 1996.
- (35) Belthangady, C. & Royer, L. A. Nat. Meth., 2019, 16, 1215-1225.
- (36) Zhang, Z., Zhang, Y., Ying, L., Sun, C. & Zhang, H. F. Machine-learning based spectral classification for spectroscopic single-molecule localization microscopy. *Opt. Lett.*, 2019, 44, 5864-5867.
- (37) Möckl, L., Roy, A. R., Petrov, P. N. & Moerner, W. E. Accurate and rapid background estimation in single-molecule localization microscopy using the deep neural network BGnet. *Proc. Natl. Acad. Sci. U. S. A.* 2020, 117, 60.

- (38) Kumar Gaire, S. *et al.* Accelerating multicolor spectroscopic single-molecule localization microscopy using deep learning. *Biomed. Opt. Express* **2020**, 11, 2705-2721.
- (39) Xu, J. et al. Super-Resolution Imaging of Higher-Order Chromatin Structures at Different Epigenomic States in Single Mammalian Cells. Cell Rep., 2018, 24, 873-882.
- (40) Agarap, A. F. Deep learning using rectified linear units (relu). *ArXiv Preprint* **2018**, 1803.08375.
- (41) Huang, B., Jones, S. A., Brandenburg, B. & Zhuang, X. Whole-cell 3D STORM reveals interactions between cellular structures with nanometer-scale resolution. *Nat. Meth.* 2008, 5, 1047-1052.
- (42) Fricke, F., Beaudouin, J., Eils, R. & Heilemann, M. One, two or three? Probing the stoichiometry of membrane proteins by single-molecule localization microscopy. *Sci. Rep.*, **2015**, **5**, 14072.
- (43) Veeraraghavan, R. & Gourdie, R. G. Stochastic optical reconstruction microscopy-based relative localization analysis (STORM-RLA) for quantitative nanoscale assessment of spatial protein organization. *Mol. Biol. Cell* 2016, 27, 3583-3590.
- (44) Faul, F., Erdfelder, E., Lang, A.-G. & Buchner, A. G*Power 3: A flexible statistical power analysis program for the social, behavioral, and biomedical sciences. *Behavior Research Methods* 2007, 39, 175-191.

- (45) Ester, M., Kriegel, H.-P., Sander, J. & Xu, X. A density-based algorithm for discovering clusters in large spatial databases with noise. *Proceedings of the Second International Conference on Knowledge Discovery and Data Mining*, **1996**, 226–231.
- (46) Kwapiszewska, K. et al. Determination of oligomerization state of Drp1 protein in living cells at nanomolar concentrations. Sci. Rep., 2019, 9, 5906.
- (47) Nieuwenhuizen, R. P. et al. Measuring image resolution in optical nanoscopy. Nat. Meth. 2013, 10, 557-562.
- (48) Song, K.-H., Zhang, Y., Wang, G., Sun, C. & Zhang, H. F. Threedimensional biplane spectroscopic single-molecule localization microscopy. *Optica* 2019, 6, 709-715.
- (49) Coltharp, C., Yang, X. & Xiao, J. Quantitative analysis of single-molecule super-resolution images. Curr. Opin. Struct. Biol., 2014, 28, 112-121.
- (50) Zhu, P. P. et al. Intra- and intermolecular domain interactions of the C-terminal GTPase effector domain of the multimeric dynamin-like GTPase Drp1. J. Biol. Chem., 2004, 279, 35967-35974.
- (51) Ovesný, M., Křížek, P., Borkovec, J., Švindrych, Z. & Hagen, G. M. ThunderSTORM: a comprehensive ImageJ plug-in for PALM and STORM data analysis and super-resolution imaging. *Bioinformatics* 2014, 30, 2389-2390.

Insert Table of Contents artwork here

